PAPER

Catalytic oxidation mechanism of ethyl acetate on O-ligand-single-atom-Ni/2-dimensional reduced graphene oxide: the essential role of the O ligand†

Xinjie Wang,[a] Juntian Li,[b] Juan Li,[b] Binghua Jing,[b] Yun Sun,[a] Teng Wang,[a] Didi Li,[a] Haibo Huang[c] and Zhimin Ao ⓘ *[b]

Ligands play an important role in the dispersion of metal and catalytic activity in single-atom transition metal-doped catalysts (SATMCs). In this work, a series of oxygen-ligand (O-ligand)-single-atom-Ni/2-dimensional reduced graphene oxide (RGO) materials (SANi$_X$-O-2DRGO ($X = 0.5–5$)) were fabricated by a simple one-step co-reduction method. The single Ni atom on SANi$_5$-O-2DRGO is embedded into the RGO and ligated by four O-ligand atoms. A systematic study confirms that the O-ligand is conducive to the dispersion of Ni and the formation of SATMCs with high metal loading. Density functional theory (DFT) calculation results demonstrate that the d-band center value of O-ligand-single-atom-Ni is closer to the Fermi level than that of the conventional N coordination, which is beneficial for electronic transition and enhances catalytic activity, i.e., the O-ligand accelerates the electron transfer between the carrier and the single metal atom, thus improving the catalytic oxidation capacity of volatile organic compounds (VOCs) on SANi$_5$-O-2DRGO. As a demonstration, SANi$_5$-O-2DRGO exhibits excellent reusability, water resistance, and stability for ethyl acetate oxidation. The degradation of ethyl acetate remained at 100% over 150 hours of continuous onstream operation. The catalytic oxidation mechanism of ethyl acetate on SANi$_5$-O-2DRGO was also investigated. The O-ligand atoms provide the key electron transfer in the activation of adsorbed oxygen and catalytic oxidation process of reaction intermediates.

1. Introduction

Volatile organic compounds (VOCs) are the main precursors of air pollution, such as urban haze and photochemical smog. VOCs are toxic, teratogenic, and carcinogenic, and can pose a great threat to human health.[1,2] Currently, catalytic oxidation is one of the most effective methods for eliminating VOCs due to its outstanding advantages, such as high catalytic activity, low reaction temperature, and less secondary pollution.[3–5] In the catalytic oxidation process of VOCs, the precious metal catalyst is costly and easily inactivated by sintering. The number of catalytic active sites for non-precious metal catalysts needs to be improved. The catalytic oxidation process is a surface reaction, and the specific surface area of the transition metal-doped catalysts exposed to the reactants is positively correlated with the catalyst activity.[6–8] The size effect is a key factor in determining catalytic performance.[9–11] The specific activity of catalysts generally increases with the dispersion in the active site.[12–14] The large size of transition metal-doped catalysts limits their widespread utilization. Developing transition metal-doped catalysts with smaller particle sizes, higher dispersion, more active sites and higher catalytic activity is the key to solving the problem.[15,16]

Single-atom transition metal-doped catalysts (SATMCs) have atomic particle sizes and highly dispersed metal sites, and appear to be a promising alternative for the catalytic oxidation of VOCs. Atomically dispersed metal easily migrates and aggregates, and it is a great challenge to obtain SATMCs with high loading capacity, good stability and high catalytic activity. The single transition metal atoms of SATMCs are commonly stabilized by covalent coordination or ionic interaction with neighboring surface atoms or bonded to heteroatoms on the support.[17,18] The single transition metal atoms facilitate electron transfer with the ligand atoms, which is one of the reasons for the high catalytic activity.[19] The ligands of transition metal-doped catalysts have been reported to induce both effective electronic and steric effects for improving activity and selectivity.[20] Nitrogen (N) is usually chosen as a ligand to disperse

[a] Guangdong Key Laboratory of Environmental Catalysis and Health Risk Control, Institute of Environmental Health and Pollution Control, School of Environmental Science and Engineering, Guangdong University of Technology, Guangzhou 510006, China

[b] Advanced Interdisciplinary Institute of Environment and Ecology, Guangdong Provincial Key Laboratory of Wastewater Information Analysis and Early Warning, Beijing Normal University, Zhuhai 519087, P. R. China. E-mail: zhimin.ao@bnu.edu.cn

[c] School of Environmental Science and Engineering, Sun Yat-sen University, Guangzhou 510275, China

† Electronic supplementary information (ESI) available. See DOI: https://doi.org/10.1039/d4ta01073f

transition metal atoms of catalysts and generate active centers.[21–25] For instance, Wang *et al.* used N ligands for anchoring Fe–N_4 sites on an FeNC catalyst to atomically disperse transition metals, revealing the role of electron transfer in pollutant degradation.[26] Although conventional ligands can disperse transition metals, the main obstacles are the lack of sufficient confinement to hold a large number of single transition metal atoms (with lower binding energy) and induce more electron transfer. This dilemma restricts the further improvement of the overall catalytic activity. Therefore, more binding energy (with greater electronegativity differences) elements are needed to hold single transition metal atoms and enhance electron transfer.

Recent investigations confirmed that the coordinated O was involved in the electron transfer process or the redox process of interfacial metal species.[27–30] Cao *et al.* discovered that O ligands are more electronegative than N ligands and can better regulate the electron transfer between charge carriers and metals.[31] In this paper, O-ligand-single-atom-Ni/2D graphene materials (SANi$_X$-O-2DRGO) are prepared for the catalytic oxidation of VOCs including ethyl acetate, *n*-hexane, and toluene. The catalytic properties of these VOCs were studied, and their reusability, water resistance and stability were explored. Specifically, SANi$_5$-O-2DRGO has high single-transition metal-atom loading and the central transition metal atoms coordinate with O-ligand atoms and steadily anchor in an RGO framework. Due to the more different electronegativity between the transition metal center, O, and carbon (C), the O-ligand accelerates the electron transfer between the carrier and the single metal atom, thus improving the catalytic oxidation capacity of VOCs on SANi$_5$-O-2DRGO. The structure and morphology of the catalysts were analyzed by high angle annular dark field scanning transmission electron microscopy (HAADF-STEM) and extended X-ray absorption fine structure spectroscopy (EXAFS). The ethyl acetate degradation pathway was studied through *in situ* diffuse reflectance infrared Fourier transform spectroscopy (DRIFTS) and *in situ* real-time TGA-GCMS. Density functional theory (DFT) calculations were also used to further explore the path of O_2 activation over the Ni–O_4 sites and to reveal the structural evolution of the bond-breaking of ethyl acetate. This study can provide new perspectives for the application of transition metal single-atom composite 2D materials.

Currently, developing low-cost and high-efficiency catalysts is necessary. In this work, the advantages of low-cost carbon materials and high-efficiency single atoms were combined by a simple one-step co-reduction method to prepare a series of SANi$_X$-O-2DRGO catalysts. The catalysts have excellent catalytic efficiency and stability for VOC oxidation. We believe that this work can provide useful references for the development of low-cost and high-efficiency catalysts for developing sustainable catalytic processes.

2. Materials and methods

2.1 Experimental reagents

Graphite powder (AR, 99.95%) was bought from Macklin, and sodium nitrate (AR, 99.0%) was purchased from General Reagents.

Potassium permanganate (AR, 99.5%), concentrated sulphuric acid (AR), concentrated hydrochloric acid (AR), hydrogen peroxide (GR), and zinc nitrate hexahydrate (AR, 99.0%) were bought from Guangzhou Chemical Reagent Factory. Manganese nitrate tetrahydrate (AR, 98.0%), ferric nitrate nonahydrate (AR, 98.0%), nickel chloride hexahydrate (AR, 98.0%), and sodium borohydride (AR, 98.0%) were obtained from Aladdin. Cobalt nitrate (AR, 99.0%) was purchased from Sigma-Aldrich.

2.2 Synthesis of SANi$_X$-O-2DRGO

SA-Ni$_X$-2DRGO was obtained by a co-reduction process with graphene oxide (GO) and the metal precursor (Fig. 1a). The graphene oxide (200 mg) and nickel chloride hexahydrate (5 mg) were dispersed in 20 mL ultrapure water by ultrasound treatment, followed by stirring overnight. Then, the solution containing 300 mg of freshly prepared NaBH$_4$ was quickly added to the above mixture while stirring. The obtained products were washed, filtered, and dried to obtain the SANi$_5$-O-2DRG. The different multiples of SANi$_X$-O-2DRGO (X = 0.5–5) were prepared by the same method with different nickel chloride hexahydrate content. SANi$_5$-O-2DRGO was selected to further study the performance and catalytic mechanism. The whole preparation process does not need high temperature treatment, and there is no expensive material. The preparation method is simple and easy to operate, and the economic benefits are remarkable. It is suitable for the batch production process for industrial application.

2.3 Characterization of SANi$_X$-O-2DRGO

In situ diffuse reflectance infrared Fourier transform spectroscopy (*In situ* DRIFTS) using a Nicolet iS 50 was performed with VOC gas to continuously detect the changes of the functional groups on the catalyst surface during the heating process. HR-TEM was carried out to analyze the microscopic morphology of
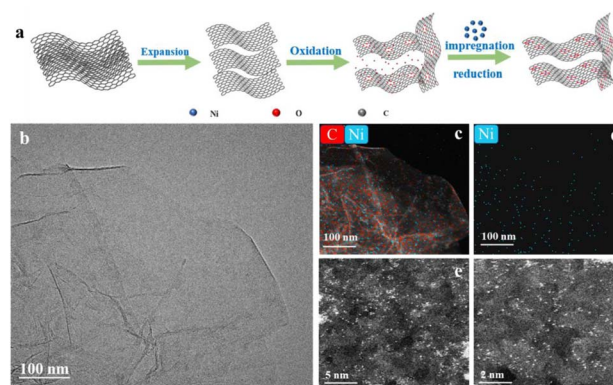

Fig. 1 (a) The preparation methods of SANi$_X$-O-2DRGO catalysts. (b) The overview TEM image of the synthesized SANi$_5$-O-2DRGO (scale bar: 100 nm). (c) The energy dispersive spectroscopy (EDS) elemental mapping of SANi$_5$-O-2DRGO (scale bar: 100 nm). (d) The Ni element distribution of SANi$_5$-O-2DRGO (scale bar: 100 nm). (e) HAADF-STEM image of a Ni single-atom on the surface of 2DRGO (scale bar: 2 nm). (f) HAADF-STEM image of a Ni single-atom on the surface of 2DRGO (scale bar: 5 nm).

the catalysts. The elemental composition and content of the material were investigated using an energy dispersive X-ray spectrometer (EDS). More detailed structural information on Ni atoms was obtained using a spherical aberration corrected high angle annular dark field scanning transmission electron microscope (HAADF-STEM, JEM-ARM300F). Ni K-edge analysis was carried out with a Si(111) crystal monochromator at the BL14W1 beamline of the Shanghai Synchrotron Radiation Facility (SSRF). X-ray absorption fine structure (XAFS) spectra of standard samples (Ni foil, NiO, and Ni_2O_3) were recorded in transmission mode. The TGA-GC/MS system consists of a TG analyzer (TGA, Mettler Toledo, Switzerland), a memory interface collector (IST16, Mettler Toledo, Switzerland), a gas chromatograph (Trace 1300, Thermo Fisher, USA), and a mass spectrometer (ISQQD, Thermo Fisher, USA). Infrared information, gas chromatographic information, and mass spectrometric information could be obtained simultaneously with the programmed temperature rise. The process stimulated the thermocatalytic reaction of the material to ethyl acetate, monitored the product species during the reaction in real time, and provided strong evidence for the analysis of the reaction pathway of ethyl acetate degradation.

2.4 Catalytic activity tests of SANi$_x$-O-2DRGO

The catalytic performance was tested using a continuous-flow fixed-bed quartz microreactor (the internal diameter is 6 mm) in combination with on-line gas chromatography (GC), and the device diagram is shown in Fig. S1.† The weight hourly space velocity (WHSV) of the catalytic reaction was 60 000 mL g^{-1} h^{-1}. 20 mg of catalyst was filled in the reactor and passed over with 500 ppm VOC gas (ethyl acetate, n-hexane, and toluene, equilibrated with dry air) at a flow rate of 20 mL min^{-1}. The water vapor with 1.5, 3.0, and 5.0 vol% was introduced into the reaction gas to analyze the water resistance of the catalysts.

The conversion of VOCs (C_{VOCs}) was calculated using the following equation:

$$C_{VOCs} (\%) = (C_0 - C_t)/C_0 \times 100\%$$

where C_0 and C_t denote the initial and the detected concentration (ppm) at time t, respectively.

The CO_2 yield (Y_{CO_2}) was defined as follows:

$$Y_{CO_2} = C_{CO_2}/C_0 \times N \times 100\%$$

where C_{CO_2} is the concentration of CO_2 (ppm) produced by the reaction. N is the number of carbon atoms in VOCs.

2.5 DFT calculations

The DMol3 module in Materials Studio software is used to perform spin-unconstrained DFT calculations.[32] The structure optimization is carried out by the exchange–correlation functional of the generalized gradient approximation and Perdew–Burke–Ernzerhof method (GGA-PBE) to minimize the energy.[33] To account for the interaction of weak van der Waals forces, DFT-D correction is performed using the method proposed by Tkatchenko and Scheffler (TS method).[34] The double numerical polarization (DNP) is selected as the atomic orbital basis set.[35]

According to the d-band model predicted by Nørskov *et al.*, the important surface parameter determining reactivity is the position of the entire d-band with respect to the Fermi level, which determines the magnitude of bonding and antibonding energy shifts.[36] The dimensions of SANi$_5$-O-2DRGO are $7 \times 7 \times 1$ and the vacuum layer which is constructed to minimize interactions between repeated surfaces is 15 Å.[37] The four C atoms of the graphene are replaced by O atoms to simulate O doping and a Ni atom is positioned on the O-doped graphene (Ni–O_4) to model the SANi$_5$-O-2DRGO.[31] The O atoms are sp^2 hybridized and form three coordinated covalent bonds with surrounding atoms.[38] The four O atoms are replaced by N atoms (Ni–N_4) to build SANi$_5$-N-2DRGO. The Brillouin zone was sampled with a $2 \times 2 \times 1$ Monkhorst–Pack k-point grid. In the process of energy convergence, the self-consistent iteration convergence deviation, the maximum interaction force, and the maximum optimization displacement are set to 2×10^{-5} Ha (1 Ha = 27.21 eV), 2×10^{-3} Ha $Å^{-1}$, and 5×10^{-3} Ha $Å^{-1}$, respectively.[39] In addition, the Mulliken method is used to calculate and analyze the charge transfer. The adsorption energy (E_{ad}) of the catalyst and ethyl acetate was calculated according to the following formula:

$$E_{ad} = E_{total} - E_{catalyst} - E_{ethylacetate}$$

where E_{total}, $E_{catalyst}$, and $E_{ethylacetate}$ represent the energy of the whole system, the catalyst substrate, and ethyl acetate, respectively. A more negative value of E_{ad} indicates a stronger interaction between the adsorbate and the substrate.

The linear synchronous transformation/quadratic synchronous transformation (LST/QST) tool and the nudged elastic band (NEB) method[40] are employed to search for the reaction transition states (TS) and minimum energy path (MEP). The energy barrier (E_{bar}) and reaction energy (ΔE) are calculated using the following equations:

$$E_{bar} = E_{TS} - E_{IS}$$

$$\Delta E = E_{FS} - E_{IS}$$

where E_{IS}, E_{TS}, and E_{FS} represent the total energy in the initial, transition, and final states, respectively.

At present, DFT calculation can only assist the verification of experimental results, and more refined and complete characterization is needed to fully match the DFT calculation with experimental techniques, including the detection of pollutants in the reaction process with higher precision and the monitoring of specific paths of oxygen transfer in the reaction process. This paper has simulated the experimental process as far as possible with the complete experimental data obtained, and the obtained results have reference value.

3. Results and discussion

3.1 SANi$_x$-O-2DRGO synthesis, morphology, and textural properties

It is reported that the thickness of a single layer of GO under atomic force microscopy (AFM) is about 1 nm.[41,42] As shown in

Fig. S2,† the thickness of GO is 1.05 nm, demonstrating that the two-dimensional GO flakes are successfully exfoliated. The infrared spectra of SANi$_5$-O-2DRGO, graphene oxide, and unreduced Ni–GO mixtures are shown in Fig. S3.† The SANi$_5$-O-2DRGO and Ni-GO mixtures appear at infrared peaks at 583 and 612 cm^{-1}, which is caused by the Ni–O vibration.[43] Compared with SANi$_5$-O-2DRGO, the Ni–O peak position in Ni–GO has shifted, probably due to the Ni element of Ni–GO not being reduced.[44]

The images of transmission electron microscopy (TEM) are displayed in Fig. 1b. The SANi$_5$-O-2DRGO framework appeared as a thin translucent gauze. Moreover, the images of HAADF-STEM and the surface sweep energy dispersive spectroscopy (EDS) of the SANi$_5$-O-2DRGO catalyst show a highly dispersive single Ni atom (Fig. 1c–f).

The atomic dispersion state and bonding configuration of Ni in SANi$_5$-O-2DRGO are further investigated by the normalized Ni K-edge X-ray absorption fine structure (XAFS) and Fourier-transformed EXAFS (FT-EXAFS). The position of the Ni K-edge is related to the Ni valence state.[31] As shown in Fig. 2a, the Ni K-edge of SANi$_5$-O-2DRGO lies between that of Ni foil and NiO, indicating the valence state of Ni in SANi$_5$-O-2DRGO is between 0 and +2. In Fig. 2b, Ni–Ni peaks are not observed in SANi$_5$-O-2DRGO at the same position with Ni foil (2.1 Å) and NiO (2.6 Å), which indicates that Ni nanoclusters are not formed. SANi$_5$-O-2DRGO has the same Ni–O bond length as NiO at 1.6 Å. According to the least squares EXAFS fitting curves (Fig. 2c) and fitting results (Table S1†), the Ni atoms are atomically dispersed on the RGO framework and the number of coordination oxygen

atoms is 4.0. Dan Li *et al.* reported that TM–O$_4$ (transition metal) doped structures have higher structural stability, lower negative formation energy, and are more easily embedded in the carrier than TM and TM–O$_3$.[45]

Based on the above results, the SANi$_5$-O-2DRGO model was constructed (Fig. 2c). The position of the d-band center (ε_d) relative to the Fermi level is an important surface parameter that determines the reactivity of the metal surface.[31] As depicted in the partial density of states (PDOS) of the Ni in Fig. 2d, the ε_d value of SANi$_5$-O-2DRGO is −1.34 eV, which is closer to the Fermi level than the conventional SANi$_5$-N-2DRGO (−1.79 eV). The ε_d of Ni in SANi$_5$-O-2DRGO is close to the Fermi level which implies that the antibonding state is less occupied. The lack of the antibonding state leads to a reduced weakening of the bonding interaction and allows for the adsorption of more electrons.[46]

The Fukui function (FF) has been widely used to predict the reaction site. FFs are classified into f_-, f_+, and f_0. f_+ reflects the ability to be attacked by nucleophiles, f_- reflects the ability to be attacked by electrophiles, and f_0 measures the ability of a certain point to be attacked by free radicals. To determine the reaction site of ethyl acetate, the FF of ethyl acetate is calculated. The two O atoms of ethyl acetate display higher Fukui values (f_-) than other atoms and will be the targets of electrophilic attack (Table S2†). Thus, ethyl acetate is likely to provide electrons to catalysts for its oxidative degradation. The adsorption properties of ethyl acetate on SANi$_5$-O-2DRGO are investigated. The optimal adsorption configurations are shown in Fig. 2e. Ethyl acetate can be stably adsorbed on the Ni site with the adsorption energy of −2.26 eV. The C1–O4 bond is stretched from 1.37 Å to 1.54 Å, which makes the molecule easy to decompose. The calculation and analysis of differential charge density can obtain the charge shift direction of materials. Fig. 2f shows that there is a charge transfer between ethyl acetate and SANi$_5$-O-2DRGO. The transfer of charge leads to the occurrence of redox reactions, so ethyl acetate will be degraded.

3.2 Catalytic performance in VOC oxidation

Ethyl acetate, toluene, and *n*-hexane are chosen as representative VOCs with different structures, *i.e.*, esters, aromatic compounds, and alkanes, respectively. The conversion efficiency and CO$_2$ yield of those three VOCs by the SANi$_5$-O-2DRGO were investigated, and the results are shown in Fig. 3c and d. The conversion of ethyl acetate is 14.8% and CO$_2$ yield is 10.5% at 280 °C by the undoped metal RGO samples, indicating their low efficiency for the oxidation of ethyl acetate.

The SANi$_X$-O-2DRGO ($X = 0.5–5$) shows a significant increase in the conversion of ethyl acetate and the yield of CO$_2$. At the same temperature, the ethyl acetate conversion rate of SANi$_X$-O-2DRGO ($X = 0.5–5$) is increased by at least 38% and at most 86%. The T_{100} (temperatures with a conversion rate of 100%) on SANi$_X$-O-2DRGO ($X = 1–5$) are all 280 °C. The difference is that the trend of T_{90} (temperatures with a conversion rate of 90%) on these five samples is SANi$_5$-O-2DRGO > SANi$_4$-O-2DRGO > SANi$_3$-O-2DRGO > SANi$_2$-O-2DRGO > SANi$_1$-O-2DRGO. The T_{50} (temperatures with a conversion rate of 50%) on SANi$_X$-O-
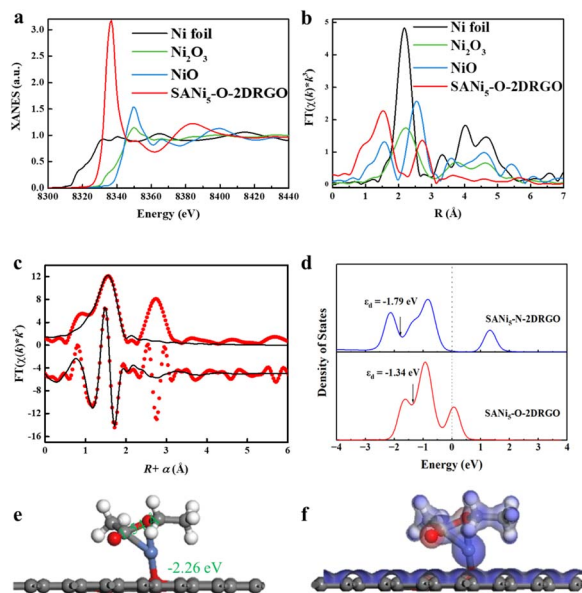

Fig. 2 (a) Ni K-edge XANES spectra. (b) FT-EXAFS at the R space for SANi$_5$-O-2DRGO, NiO, and Ni foil. (c) EXAFS fitting curves of SANi$_5$-O-2DRGO. (d) PDOS of Ni among SANi$_5$-O-2DRGO and SANi$_5$-N-2DRGO. (e) Optimal adsorption configurations of ethyl acetate on SANi$_5$-O-2DRGO. (f) Charge density distribution of ethyl acetate on SANi$_5$-O-2DRGO (the red cloud indicates electron enrichment and blue cloud indicates electron deficiency).
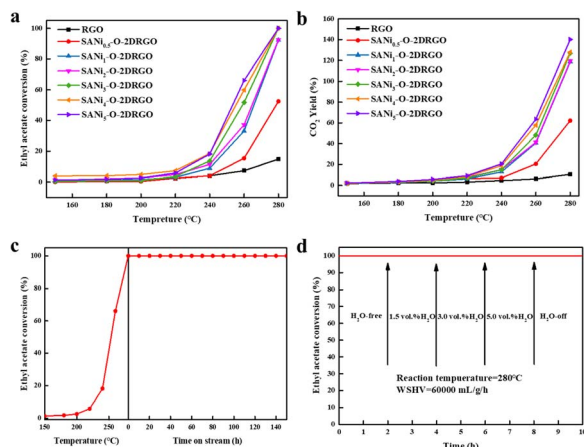
Fig. 3 Catalytic performances of $SANi_X$-O-2DRGO ($X = 0.5-5$). (a) Conversion of ethyl acetate over $SANi_X$-O-2DRGO ($X = 0.5-5$) with different Ni loadings at different temperatures. (b) CO_2 yield. (c) Catalytic stability of $SANi_5$-O-2DRGO. (d) Effect of water vapor on the ethyl acetate conversion over $SANi_5$-O-2DRGO at 280 °C.

2DRGO ($X = 1-5$) is 265, 264, 259, 255, and 250 °C, and $SANi_5$-O-2DRGO has the lowest T_{50}. The increase of conversion rate is closely related to the content of Ni metal. The ICP-MS results are shown in Table S3;† the actual content of Ni is 0.73%, 1.86%, 3.43%, 5.44%, 8.13%, and 10.16%, respectively. It can be seen that the catalytic performance increases gradually with the increased content of Ni metal at the same temperature. Typically, $SANi_5$-O-2DRGO has the best catalytic performance, which shows nearly 100% conversion of ethyl acetate and CO_2 yield at 280 °C. Therefore, $SANi_5$-O-2DRGO is selected to further study the performance and catalytic mechanism.

$SANi_5$-O-2DRGO also shows excellent catalytic performance in the degradation of n-hexane and toluene. The temperature of

100% conversion of toluene (Fig. S9†) and n-hexane (Fig. S10†) is 280 °C and 320 °C, respectively. In contrast, RGO shows only 8.9% and 8.8% conversion of n-hexane and toluene at the same temperature. The above results show that $SANi_X$-O-2DRGO ($X = 0.5-5$) exhibits great stability and reusability for the low temperature catalytic oxidation of various VOCs.

3.3 Degradation mechanism and pathway of VOCs on $SANi_5$-O-2DRGO

X-ray photoelectron spectroscopy (XPS) is used to determine the elemental composition and the chemical valence in the fresh and used $SANi_5$-O-2DRGO. As presented in Fig. S13,† split peak fit plots of the C 1s peak, O 1s peak, and Ni 2p peak of fresh and used $SANi_5$-O-2DRGO are analyzed. The C 1s peak is divided into C–C bonds with sp^2 orbital hybridization, C–C bonds with sp^3 orbital hybridization, and C=O–O (Fig. 4a).[47,48] The C–C bond binding energies with sp^2 hybridization of fresh and used $SANi_5$-O-2DRGO are 284.02 eV and 283.94 eV, and C–C bonds with sp^3 orbital hybridization are distributed at 285.04 eV and 284.86 eV.[49] The C=O–O bond binding energies of fresh and used $SANi_5$-O-2DRGO are 288.16 eV and 288.77 eV, respectively. There is no significant change in the C 1s orbital binding energy of the catalyst after the use. It is noteworthy that the atomic percentage of sp^2 hybridized C–C bonds changes significantly after the use from 16.16% to 7.47%. This may be due to some non-carbon atoms covalently bound to the $SANi_5$-O-2DRGO carbon atoms during the reaction.[50] The difference in the type of these non-carbon atoms affects the charge distribution of $SANi_5$-O-2DRGO, which is consistent with the reduction in the extent of defects after the reaction shown in the Raman test results. The slight changes of the Raman test result after use might slightly affect the overall catalytic activity of the catalyst.
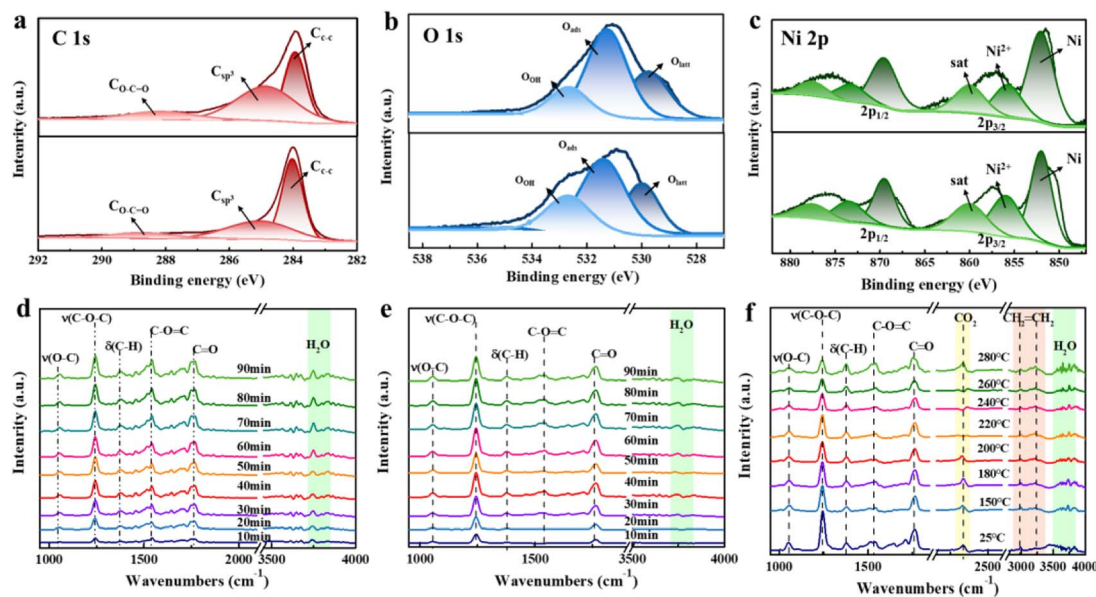

Fig. 4 XPS spectra of fresh and used $SANi_5$-O-2DRGO: (a) C 1s, (b) O 1s, and (c) Ni 2p. (d) *In situ* DRIFTS spectra of RGO at 25 °C after different reaction times. (e) *In situ* DRIFTS spectra of $SANi_5$-O-2DRGO at 25 °C after different reaction times and (f) at temperatures ranging from 25 °C to 280 °C.

The peaks of O 1s can be divided into the oxygen ligands of metal (M–O), adsorbed oxygen (O_{ads}), and surface hydroxyl (O_{OH}).[51] It can be seen in Fig. 4b that for fresh SANi$_5$-O-2DRGO, the peak at 529.73 eV is the O ligand bound to Ni.[52] The peak at 531.25 eV can be classified as a large number of defective sites with low oxygen coordination, which can be attributed to adsorbed oxygen species (*e.g.* O^{2-}, O_2^{2-}, or O^-).[53] The peak at the 532.65 eV position is associated with hydroxyl species that adsorb water molecules on the surface, indicating a good affinity of SANi$_5$-O-2DRGO for oxygen. Compared with the fresh SANi$_5$-O-2DRGO, the positions of the Ni–O peak, O_{ads}, and O_{OH} on used SANi$_5$-O-2DRGO are located at 529.99 eV, 531.40 eV, and 532.68 eV, which were almost unchanged. Interestingly, the percentage of O_{ads} decreases by 6.5% after use, which is related to the involvement of defective sites with low oxygen coordination on the O_{ads} in the degradation reaction.

Besides, the valence state of the element Ni is also investigated. In the fine spectrum of the Ni 2p orbital, three peaks are fitted to each of the fresh and used SANi$_5$-O-2DRGO (Fig. 4c). The binding energy peaks are 852.01 eV and 852.00 eV for the Ni(0), and 855.68 eV and 855.93 eV for the Ni(II). The satellite peaks of Ni(II) are located at 859.96 eV and 860.01 eV.[54,55] The comparison shows that the binding energy positions of Ni(0) and Ni(II) remain similar for fresh and used SANi$_5$-O-2DRGO, although there is a slight shift in the Ni(0)/Ni(II) ratio after the reaction, from 2.5 to 2.3. Combined with the H$_2$-TPR results, Ni is the active site of the reaction. Therefore, in the reaction, Ni is involved in the reduction oxidation process, and is oxidised from Ni(0) to Ni(II), and is eventually reduced to Ni(0).

To infer the intermediates of the degradation pathway, *in situ* DRIFTS is used to study the changes of the functional groups on the surface of SANi$_5$-O-2DRGO during the catalytic oxidation of ethyl acetate. Fig. 4d and e show the changes of the functional groups on the RGO and SANi$_5$-O-2DRGO surface in ethyl acetate at 25 °C. The peaks at 1058 and 1246 cm^{-1} are associated with the absorption of the bending vibrations v(C–C–O) and v(C–O) of esters.[56] The peaks near 1558 and 1752 cm^{-1} are caused by the O–C=O anti-stretching vibration and the C=O stretching vibration of esters.[57] With increasing reaction time, the peaks at 1058, 1246, 1558, and 1752 cm^{-1} show the same increasing trend, which indicates the four peaks associated with the adsorption of ethyl acetate. Fig. 4f shows the DRIFTS spectra obtained after the reaction had stabilized at 30, 150, 180, 200, 220, 240, 260, and 280 °C for 30 min, respectively, while maintaining the same experimental conditions. It can be seen clearly that the bending vibration peaks around 1058 cm^{-1} for v(C–O–C) and 1246 cm^{-1} for v(C–O) of esters show a decreasing trend with increasing reaction temperature. This is probably due to the desorption and degradation of the ethyl acetate adsorbed on the surface of the SANi$_5$-O-2DRGO as the reaction temperature increases. The peak at 1378 cm^{-1} is the stretching vibration of δ(C–H), which belongs to the primary alcohol.[58–61] The δ(C–H) of the primary alcohol shows a rapid increase at 260–280 °C, which may be related to the formation of the intermediate product ethanol. The stretching vibration peaks around 1558 cm^{-1} for O–C=O and 1752 cm^{-1} for C=O show a trend of decreasing and then increasing with the increase of

the reaction temperature. This indicates that the ethyl acetate adsorbed on the surface of SANi$_5$-O-2DRGO is degraded during the reaction. When the temperature increases, intermediate products with an aldehyde group and carboxylic acid in the same functional group are formed. The large peak in the 2230–2400 cm^{-1} band is CO$_2$ in the gaseous state, which shows a decreasing and then increasing trend with increasing reaction time and temperature. This is the result of the CO$_2$ desorption during the reaction, but the increasing CO$_2$ is produced by the mineralization of ethyl acetate as the temperature increases.

In situ real-time TGA/DSC-IR-GCMS and DFT calculations are combined to infer the reaction pathways for the catalytic oxidation of ethyl acetate on SANi$_5$-O-2DRGO. Combined with the *in situ* DRIFTs, $C_4H_6O_2$, $C_2H_4O_2$, C_2H_6O, C_2H_4O, C_2H_2O, C_2H_4, CH_2O_2, CO_2, and H_2O are the possible intermediates. Gas samples collected at 30 °C show these fragment peaks in mass spectra ($C_4H_8O_2$, m/z = 88, 70, and 43), indicating the presence of ethyl acetate (Fig. S14†). As shown in Fig. 5a–f, the intermediate product detected by these gas signals at 270 °C is presumed to be ethanol (C_2H_6O, m/z = 46, 45 and 31), acetic acid (C_7H_6O, m/z = 60, 45 and 43), ketene (C_2H_2O, m/z = 42, 41 and 30), ethylene (C_2H_4, m/z = 29, 26 and 24), formic acid (CH_2O_2, m/z = 46, 45 and 29), and formaldehyde (C_2H_4O, m/z = 44, 43 and 29). Information on all detected intermediates during the reaction is presented in Table S5.†

The bond-breaking reaction catalyzed on SANi$_5$-O-2DRGO plays a crucial role in the decomposition of ethyl acetate.[62] To elucidate the mechanism, the potential energy surface and
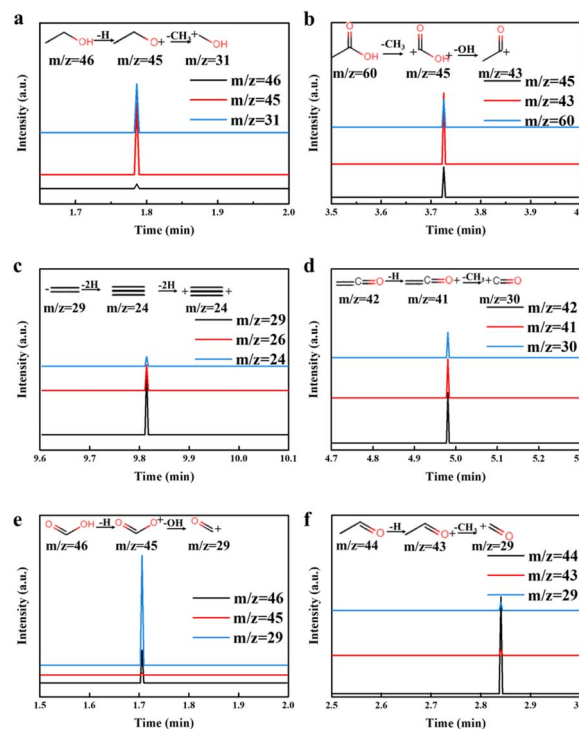

Fig. 5 The mass spectroscopy of reaction intermediates including ethanol (a), acetic acid (b), ketene (c), formic acid (d), ethylene (e), and formaldehyde (f) during the catalytic degradation of ethyl acetate over SANi$_5$-O-2DRGO.
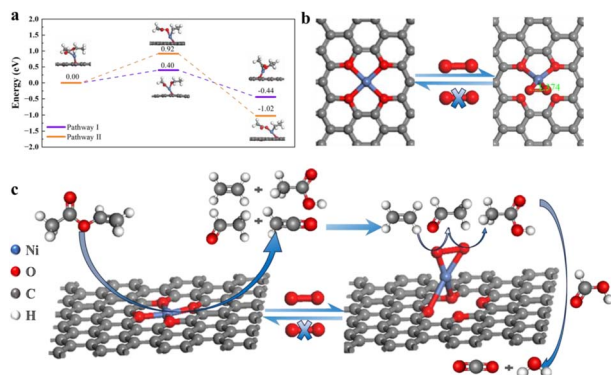
Fig. 6 (a) The energy pathways and structural evolution of intermediates. (b) Schematic diagram of adsorbed oxygen activated at the Ni site. (c) The possible reaction mechanism for the degradation of ethyl acetate by SANi$_5$-O-2DRGO.

structural evolution for the bond-breaking of ethyl acetate on SANi$_5$-O-2DRGO are analyzed by DFT calculations based on experimental data. Fig. 6a illustrates two possible reaction pathways along with their respective relative energies.

In pathway I, the ethyl acetate adsorbed on SANi$_5$-O-2DRGO is first broken across the C1–O4 bond to form the CH$_3$CO–Ni–OC$_2$H$_5$ species with the energy barrier of 0.40 eV. Subsequently, the H9 atom migrates from the C2 atom to O4, leading to the production of CH$_2$CO and C$_2$H$_5$OH.

In pathway II, the O4–C5 of ethyl acetate is inserted by Ni to produce CH$_3$COO–Ni–C$_2$H$_5$ with an energy barrier of 0.92 eV. Following this, the H13 atom migrates from the C6 atom to O4, giving rise to the generation of CH$_3$COOH and C$_2$H$_4$. According to transition state theory, both of the above reactions are expected to occur readily at a temperature of 550 K. As a result, they can coexist and take place simultaneously under the experimental conditions at this temperature. As the reaction proceeds, oxygen is adsorbed and activated at the Ni sites of SANi$_5$-O-2DRGO. The O–O bond length is stretched from 1.22 Å to 1.37 Å and 0.5 electron is obtained from O-ligand atoms and Ni atoms (Fig. 6b). Next, the above intermediate products are adsorbed for the following oxidation reaction: C$_2$H$_5$OH/C$_2$H$_4$ → CH$_3$CHO → CH$_3$COOH → HCOOH → CO$_2$ and H$_2$O. The corresponding electron transfers are listed in Table 1. Electrons are gradually transferred from SANi$_5$-O-2DRGO to O$_2$ and eventually oxidize the compounds to CO$_2$ and H$_2$O.

In summary, a possible reaction mechanism for the degradation of ethyl acetate on SANi$_5$-O-2DRGO is shown in Fig. 6c. Firstly, the ethyl acetate molecule is chemically adsorbed by Ni on the catalyst at elevated temperatures. Ethyl acetate is firstly converted to CH$_3$COO–Ni–C$_2$H$_5$ or CH$_3$CO–Ni–OC$_2$H$_5$, and then these via bond breaking reform CH$_2$CO, C$_2$H$_5$OH or CH$_3$COOH, C$_2$H$_4$. At the same time, the oxygen molecules adsorbed on the surface of the SANi$_5$-O-2DRGO are activated by Ni anchored on the graphene to form an active low coordination oxygen excited state. CH$_2$CO and C$_2$H$_4$ are oxidized to CH$_3$COOH and CH$_3$CHO. Finally, these are oxidized to CO$_2$ and H$_2$O by activated oxygen molecules. As the activated oxygen is consumed, the catalyst is reduced to Ni(0), creating an oxygen vacancy. With the generation of the oxygen vacancy, the oxygen adsorbed on the surface with the low coordination participates in the reaction, and the XPS results show that the percentage of adsorbed oxygen decreases after the reaction. The adsorbed oxygen molecules are activated to form an active low coordination oxygen excited state to participate in the reaction. The used SANi$_5$-O-2DRGO showed a slight shift in Ni 2p and maintained similar ratio of Ni(0)/Ni(II) to the fresh SANi$_5$-O-2DRGO. Ni(II) is reduced to Ni(0) after participating in the reaction, and then oxidized to Ni(II) to continue to participate in the reaction, forming a Ni(0)/Ni(II) redox cycle. Therefore, the catalytic oxidation mechanism of ethyl acetate on SANi$_5$-O-2DRGO catalysts follows the Eley–Rideal (E–R) model.

The results of DFT calculations are consistent with the degradation path predicted by the experimental results and reveal the micro-degradation mechanism. Therefore, two possible pathways for ethyl acetate to be degraded on SANi$_5$-O-2DRGO are proposed (Fig. 7). However, according to the DFT calculation of the reaction energy barrier in the two paths and the DRIFTS spectra change intensity, it is speculated that the degradation of ethyl acetate on SANi$_5$-O-2DRGO is more inclined to pathway I. The catalytic degradation pathway of ethyl acetate on SANi$_5$-O-2DRGO can be represented by the following chemical equation:
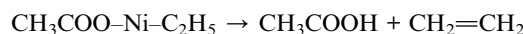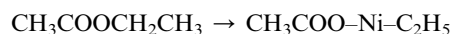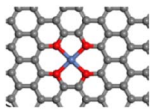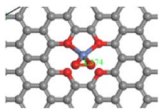
Pathway I:

$$CH_3COOCH_2CH_3 \rightarrow CH_3COO\text{–}Ni\text{–}C_2H_5$$

$$CH_3COO\text{–}Ni\text{–}C_2H_5 \rightarrow CH_3COOH + CH_2\text{=}CH_2$$
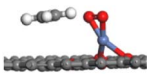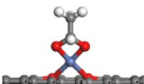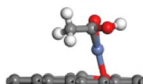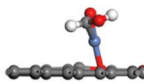
Table 1 The electron transfer between Ni–O$_4$ and O$_2$

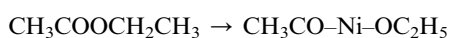| SANi$_5$-O-2DRGO						
Ni	0.47 eV	0.63 eV	0.64 eV	0.64 eV	0.40 eV	0.39 eV
O1	−0.57 eV	−0.56 eV	−0.56 eV	−0.55 eV	−0.47 eV	−0.47 eV
O2	−0.57 eV	−0.49 eV	−0.49 eV	−0.47 eV	−0.45 eV	−0.45 eV
O3	−0.57 eV	−0.56 eV	−0.56 eV	−0.55 eV	−0.44 eV	−0.44 eV
O4	−0.57 eV	−0.49 eV	−0.49 eV	−0.47 eV	−0.44 eV	−0.44 eV
O5	—	−0.25 eV	−0.26 eV	−0.55 eV	−0.48 eV	−0.47 eV
O6	—	−0.25 eV	−0.26 eV	−0.55 eV	−0.37 eV	−0.37 eV
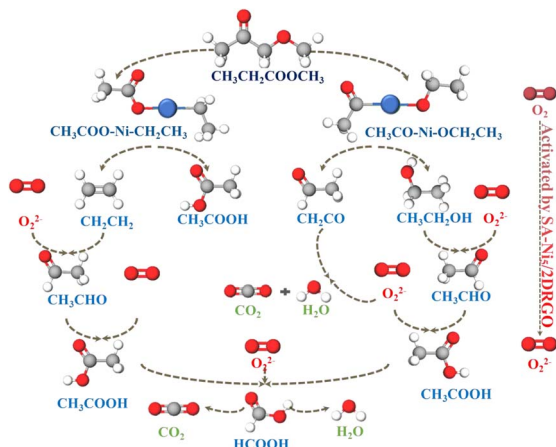
Fig. 7 The possible degradation pathway of ethyl acetate on $SANi_5$-O-2DRGO.

$$2CH_2=CH_2 + O_2^{2-} \rightarrow 2CH_3CHO$$

Pathway II:

$$CH_3COOCH_2CH_3 \rightarrow CH_3CO-Ni-OC_2H_5$$

$$CH_3CO-Ni-OC_2H_5 \rightarrow CH_2CO + CH_3CH_2OH$$

$$CH_2CO + O_2^{2-} \rightarrow CO_2 + H_2O$$

$$2CH_3CH_2OH + O_2^{2-} \rightarrow 2CH_3CHO + H_2O$$
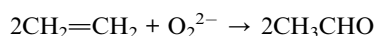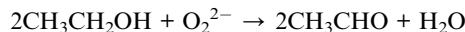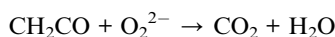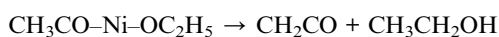
Pathways I and II together:

$$2CH_3CHO + O_2^{2-} \rightarrow 2CH_3COOH$$

$$CH_3COOH + O_2^{2-} \rightarrow HCOOH + CO_2 + H_2O$$

$$HCOOH \rightarrow CO_2 + H_2O$$
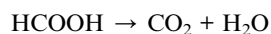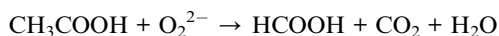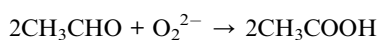
4. Conclusions

In this work, $SANi_X$-O-2DRGO (X = 0.5–5) catalysts were prepared by a simple one-step co-reduction method. $SANi_5$-O-2DRGO has high single-transition metal-atom loading and stable structure. The position of the d-band center of $SANi_5$-O-2DRGO (-1.34 eV) is closer to the Fermi level than that of $SANi_5$-N-2DRGO (-1.79 eV), and the bonding state between the $SANi_5$-O-2DRGO and the intermediate becomes stronger. Compared with traditional N ligand single-atom catalysts, $SANi_5$-O-2DRGO catalysts have better charge transfer ability between the carrier and the single metal atom, enhancing the catalytic activity. $SANi_5$-O-2DRGO is able to degrade ethyl acetate with stable performance at an air speed of 60 000 mL g^{-1} h^{-1} for 150 hours. The catalytic oxidation mechanism of ethyl acetate on $SANi_5$-O-2DRGO catalysts follows the Eley–Rideal (E–

R) model. The O-ligand atoms transfer electrons to adsorbed oxygen forming activated oxygen to oxidize the intermediates. When the activated oxygen is consumed, the catalyst is reduced to Ni(0), creating an oxygen vacancy, forming a Ni(0)/Ni(II) redox cycle. Further improving the catalytic performance and yield of non-noble metal single-atom catalysts is still an important issue. However, we believe that this study can provide a new idea for the design and application of O-ligand-single-atom catalysts.

Conflicts of interest

There are no conflicts to declare.

Acknowledgements

Notes and references

1 M. Hakim, Y. Broza, O. Barash, N. Peled, M. Phillips, A. Amann and H. Haick, Volatile organic compounds of lung cancer and possible biochemical pathways, *Chem. Rev.*, 2012, **112**, 5949–5966, DOI: **10.1021/cr300174a**.

2 B. Li, S. S. H. Ho, X. Li, L. Guo, A. Chen, L. Hu, Y. Yang, D. Chen, A. Lin and X. Fang, A comprehensive review on anthropogenic volatile organic compounds (VOCs) emission estimates in China: Comparison and outlook, *Environ. Int.*, 2021, **156**, 106710, DOI: **10.1016/j.envint.2021.106710**.

3 Z. Xu, Z. Ao, M. Yang and S. Wang, Recent progress in single-atom alloys: Synthesis, properties, and applications in environmental catalysis, *J. Hazard. Mater.*, 2022, **424**, 127427, DOI: **10.1016/j.jhazmat.2021.127427**.

4 G. Liu, J. Zhou, W. Zhao, Z. Ao and T. An, Single atom catalytic oxidation mechanism of formaldehyde on Al doped graphene at room temperature, *Chin. Chem. Lett.*, 2020, **31**, 1966–1969, DOI: **10.1016/j.cclet.2019.12.023**.

5 S. Song, S. Zhang, X. Zhang, P. Verma and M. Wen, Advances in catalytic oxidation of volatile organic compounds over Pd-supported catalysts: recent trends and challenges, *Front. Mater.*, 2020, **7**, 595567, DOI: **10.3389/fmats.2020.595667**.

6 P. Yang, J. Li and S. Zuo, Promoting oxidative activity and stability of CeO_2 addition on the MnO_x modified kaolin-based catalysts for catalytic combustion of benzene, *Chem. Eng. Sci.*, 2017, **162**, 218–226, DOI: **10.1016/j.ces.2017.01.009**.

7 D. Li, C. Li and K. Suzuki, Catalytic oxidation of VOCs over Al and Fe-pillared montmorillonite, *Appl. Clay Sci.*, 2013, **77–78**, 56–60, DOI: **10.1016/j.clay.2013.02.027**.

8 J. Li, S. Wang and Z. Ao, Environmental surfaces and interfaces: A forward position to the future of environmental research, *Environ. Surf. Interfaces*, 2023, **1**, 1–2, DOI: **10.1016/j.esi.2023.04.001**.

9 D. Liu, S. Ding, S. Feng, H. Tian, H. Yan, T. Li, D. Du, P. Liu, M. Shao and Y. Lin, Two-dimensional single-atom catalyst with optimized iron-sites produced by thermal melting of metal-mrganic-frameworks for oxygen reduction reaction, *Small Methods*, 2020, **4**, 1900827, DOI: **10.1002/smtd.201900827**.

10 W. Wei and X. Xua, Well-elaborated, mechanochemically synthesized Fe-TPP⊂ZIF precursors to atomically dispersed iron-nitrogen species for oxygen reduction reaction and Zn-air batteries, *Nano Energy*, 2018, **2**, 29–31, DOI: **10.1016/j.nanoen.2018.07.033**.

11 X. Zheng, P. Li, S. Dou, W. Sun, H. Pan, D. Wang and Y. Li, Non-carbon-supported single-atom site catalysts for electrocatalysis, *Energy Environ. Sci.*, 2021, **14**, 2809–2858, DOI: **10.1039/D1EE00248A**.

12 Z. Jiang, X. Feng, J. Deng, C. He, M. Douthwaite, Y. Yu, J. Liu, Z. Hao and Z. Zhao, Atomic-scale insights into the low-temperature oxidation of methanol over a single-atom Pt_1-Co_3O_4 catalyst, *Adv. Funct. Mater.*, 2019, **29**, 1902041, DOI: **10.1002/adfm.201902041**.

13 P. Huang, J. Huang, S. A. Pantovich, A. D. Carl, T. G. Fenton, C. A. Caputo, R. L. Grimm, A. I. Frenkel and G. Li, Selective CO_2 reduction catalyzed by single cobalt sites on carbon nitride under visible-light irradiation, *J. Am. Chem. Soc.*, 2018, **140**, 16042–16047, DOI: **10.1021/jacs.8b10380**.

14 Z. Hou, L. Dai, Y. Liu, J. Deng, L. Jing, W. Pei, R. Gao, Y. Feng and H. Dai, Highly efficient and enhanced sulfur resistance supported bimetallic single-atom palladium–cobalt catalysts for benzene oxidation, *Appl. Catal., B*, 2021, **285**, 119844, DOI: **10.1016/j.apcatb.2020.119844**.

15 C. Jia, S. Li, Y. Zhao, W. Ren, X. Chen, Z. Su, W. Yang, Y. Wang, S. Zheng, F. Pan and C. Zhao, Nitrogen vacancy induced coordinative reconstruction of single-atom Ni catalyst for efficient electrochemical CO_2 reduction, *Adv. Funct. Mater.*, 2021, **31**, 2107072, DOI: **10.1002/adfm.202107072**.

16 H. John Jones, T. DeLaRiva, J. Peterson, H. Pham, R. Challa, G. Qi, H. Wiebenga, Y. Wang and A. Datye, Thermally stable single-atom platinum-on-ceria catalysts via atom trapping, *Science*, 2023, **353**, 6295, DOI: **10.1126/science.aaf8800**.

17 X. Cui, W. Li, P. Ryabchuk, K. Junge and M. Beller, Bridging homogeneous and heterogeneous catalysis by heterogeneous single-metal-site catalysts, *Nat. Catal.*, 2018, **1**, 385–397, DOI: **10.1038/s41929-018-0090-9**.

18 Q. Li, B. Liu and Z. Ao, Photocatalytic degradation of typical VOCs on sulfur-doped porous graphene, *Chin. Sci. Bull.*, 2022, **67**, 976–985, DOI: **10.1360/TB-2021-1042**.

19 Y. Chen, S. Ji, W. Sun, Y. Lei, Q. Wang, A. Li, W. Chen, G. Zhou, Z. Zhang, Y. Wang, L. Zheng, Q. Zhang, L. Gu, X. Han, D. Wang and Y. Li, Engineering the atomic interface with single platinum atoms for enhanced photocatalytic hydrogen production, *Angew Chem. Int. Ed. Engl.*, 2020, **59**, 1295–1301, DOI: **10.1002/anie.201912439**.

20 Y. Zou, J. Hu, B. Li, L. Lin, Y. Li, F. Liu and X. Li, Tailoring the coordination environment of cobalt in a single-atom catalyst through phosphorus doping for enhanced activation of peroxymonosulfate and thus efficient degradation of sulfadiazine, *Appl. Catal., B*, 2022, **312**, 121408, DOI: **10.1016/j.apcatb.2022.121408**.

21 M. Zhou, Y. Jiang, G. Wang, W. Wu, W. Chen, P. Yu, Y. Lin, J. Mao and L. Mao, Single-atom Ni-N_4 provides a robust cellular NO sensor, *Nat. Commun.*, 2020, **11**, 3188, DOI: **10.1038/s41467-020-17018-6**.

22 Q. Chen, Y. Liu, Y. Lu, Y. Hou, X. Zhang, W. Shi and Y. Huang, Atomically dispersed Fe/Bi dual active sites single-atom nanozymes for cascade catalysis and peroxymonosulfate activation to degrade dyes, *J. Hazard. Mater.*, 2022, **422**, 126929, DOI: **10.1016/j.jhazmat.2021.126929**.

23 X. Li, X. Huang, S. Xi, S. Miao, J. Ding, W. Cai, S. Liu, X. Yang, H. Yang, J. Gao, J. Wang, Y. Huang, T. Zhang and B. Liu, Single cobalt atoms anchored on porous N-doped graphene with dual reaction sites for efficient fenton-like catalysis, *J. Am. Chem. Soc.*, 2018, **140**, 12469–12475, DOI: **10.1021/jacs.8b05992**.

24 Z. Guo, Y. Xie, J. Xiao, Z. Zhao, Y. Wang, Z. Xu, Y. Zhang, L. Yin, H. Cao and J. Gong, Single-atom Mn-N_4 site-catalyzed peroxone reaction for the efficient production of hydroxyl radicals in an acidic solution, *J. Am. Chem. Soc.*, 2019, **141**, 12005–12010, DOI: **10.1021/jacs.9b04569**.

25 Y. Gao, X. Duan, B. Li, Q. Jia, Y. Li, X. Fan, F. Zhang, G. Zhang, S. Wang and W. Peng, Fe containing template derived atomic Fe-N-C to boost Fenton-like reaction and charge migration analysis on highly active Fe-N_4 sites, *J. Mater. Chem. A*, 2021, **9**, 14793–14805, DOI: **10.1039/D1TA02446A**.

26 L. Zhang, Y. Sun, R. Ge, W. Zhou, Z. Ao and J. Wang, Mechanical insight into direct singlet oxygen generation pathway: Pivotal role of FeN_4 sites and selective organic contaminants removal, *Appl. Catal., B*, 2023, **339**, 123130, DOI: **10.1016/j.apcatb.2023.123130**.

27 K. Graciani, F. Xu, E. Baber, J. Evans, D. S. Senanayake, P. Liu, J. Hrbek and J. Sanz, Highly active copper-ceria and copper-ceria-titania catalysts for methanol synthesis from CO_2, *Science*, 2014, **345**, 6196, DOI: **10.1126/science.1253057**.

28 W. Karim, C. Spreafico, A. Kleibert, J. Gobrecht, J. VandeVondele, Y. Ekinci and J. Bokhoven, Catalyst support effects on hydrogen spillover, *Nature*, 2017, **541**, 68–71, DOI: **10.1038/nature20782**.

29 C. Xu, G. Chen, Y. Zhao, P. Liu, X. Duan, L. Gu, G. Fu, Y. Yuan and N. Zheng, Interfacing with silica boosts the catalysis of copper, *Nat. Commun.*, 2018, **9**, 3367, DOI: **10.1038/s41467-018-05757-6**.

30 X. Zheng, Y. Ji, J. Tang, J. Wang, B. Liu, H. Steinrück, K. Lim, Y. Li, M. Toney, K. Chan and Y. Cui, Retraction note: theory-guided Sn/Cu alloying for efficient CO_2 electroreduction at low overpotentials, *Nat. Catal.*, 2021, **4**, 441, DOI: **10.1038/s41929-021-00619-9**.

31 Z. Zhou, W. Li, Z. Zhang, Q. Huang, X. Zhao and W. Cao, Ni-O_4 as active sites for efficient oxygen evolution reaction with

electronic metal-support interactions, *ACS Appl. Mater. Interfaces*, 2022, **14**, 47542–47548, DOI: **10.1021/acsami.2c11201**.

32 B. Delley, From molecules to solids with the DMol3 approach, *J. Chem. Phys.*, 2000, **113**, 7756–7764, DOI: **10.1063/1.1316015**.

33 K. J. P. Perdew and M. Ernzerhof, Generalized gradient approximation made simple, *Phys. Rev. Lett.*, 1996, **77**, 3865–3868, DOI: **10.1103/PhysRevLett.77.3865**.

34 A. Tkatchenko and M. Scheffler, Accurate molecular van der waals interactions from ground-state electron density and free-atom reference data, *Phys. Rev. Lett.*, 2009, **102**, 073005, DOI: **10.1103/PhysRevLett.102.073005**.

35 B. Delley, An all-electron numerical method for solving the local density functional for polyatomic molecules, *J. Chem. Phys.*, 1990, **92**, 508–517, DOI: **10.1063/1.458452**.

36 B. Norskov, Electronic factors determining the reactivity of metal surfaces, *Surf. Sci.*, 1995, **343**, 211–220, DOI: **10.1016/0039-6028(96)80007-0**.

37 Z. Ao, S. Li and Q. Jiang, Thermal stability of interaction between the CO molecules and the Al doped graphene, *Phys. Chem. Chem. Phys.*, 2009, **11**, 1683–1687, DOI: **10.1039/B812188E**.

38 H. Yin, L. Gan and P. Wang, The identification of optimal active boron sites for N_2 reduction, *J. Mater. Chem. A*, 2020, **8**, 3910–3917, DOI: **10.1039/C9TA13700A**.

39 Y. Su, W. Li, G. Li, Z. Ao and T. An, Density functional theory investigation of the enhanced adsorption mechanism and potential catalytic activity for formaldehyde degradation on Al-decorated C_2N monolayer, *Chin. J. Catal.*, 2019, **40**, 664–672, DOI: **10.1016/S1872-2067(18)63201-2**.

40 G. Henkelman, B. Uberuaga and H. Jónsson, A climbing image nudged elastic band method for finding saddle points and minimum energy paths, *J. Chem. Phys.*, 2000, **113**, 9901–9904, DOI: **10.1063/1.1329672**.

41 K. Novoselov, A. Geim, S. Morozov, D. Jiang, Y. Zhang, S. Dubonos, I. Grigorieva and A. Firsov, Electric field effect in atomically thin carbon films, *Science*, 2004, **306**, 666–669, DOI: **10.1126/science.1102896**.

42 A. Geim and K. Novoselov, The rise of graphene, *Nat. Mater.*, 2007, **6**, 183–191, DOI: **10.1038/nmat1849**.

43 M. Seehra and V. Singh, Magnetic ordering of nickel hydroxide layers 30 A apart obtained by intercalating dodecyl sulfate, *J. Phys.: Condens.Matter*, 2013, **25**, 356001, **http://stacks.iop.org/JPhysCM/25/356001**.

44 R. Liu, S. Liang, X. Tang, D. Yan, X. Li and Z. Yu, Tough and highly stretchable graphene oxide/polyacrylamide nanocomposite hydrogels, *J. Mater. Chem. A*, 2012, **22**, 14160–14167, DOI: **10.1039/C2JM32541A**.

45 J. Meng, D. Li, Y. Niu, H. Zhao, C. Liang and Z. He, Structural, electronic, and magnetic properties of 3D metal trioxide and tetraoxide superhalogen cluster-doped monolayer BN, *Phys. Lett. A*, 2016, **380**, 2300–2306, DOI: **10.1016/j.physleta.2016.04.042**.

46 Z. Chen, Y. Song, J. Cai, X. Zheng, D. Han, Y. Wu, Y. Zang, S. Niu, Y. Liu, J. Zhu, X. Liu and G. Wang, Tailoring the d-band centers enables Co_4N Nanosheets to be highly active

for hydrogen evolution catalysis, *Angew. Chem., Int. Ed.*, 2018, **57**, 5076–5080, DOI: **10.1002/anie.201801834**.

47 P. Chen, J. Sodhi, Y. Qiu, T. Valentin, R. Steinberg, Z. Wang, R. Hurt and I. Wong, Multiscale graphene topographies programmed by sequential mechanical deformation, *Adv. Mater.*, 2016, **28**, 3564–3571, DOI: **10.1002/adma.201506194**.

48 H. Jeong, H. Noh, J. Kim, M. Jin, C. Park and Y. Lee, X-ray absorption spectroscopy of graphite oxide, *Europhys. Lett.*, 2008, **82**, 67004, DOI: **10.1209/0295-5075/82/67004**.

49 A. Kovtun, D. Jones, S. Dell, E. Treossi, A. Liscio and V. Palermo, Accurate chemical analysis of oxygenated graphene-based materials using X-ray photoelectron spectroscopy, *Carbon*, 2019, **143**, 268–275, DOI: **10.1016/j.carbon.2018.11.012**.

50 C. Soldano, A. Mahmood and E. Dujardin, Production, properties and potential of graphene, *Carbon*, 2010, **48**, 2127–2150, DOI: **10.1016/j.carbon.2010.01.058**.

51 H. Arandiyan, H. Dai, J. Deng, Y. Liu, B. Bai, Y. Wang, X. Li, S. Xie and J. Li, Three-dimensionally ordered macroporous $La_{0.6}Sr_{0.4}MnO_3$ with high surface areas: active catalysts for the combustion of methane, *J. Catal.*, 2013, **307**, 327–339, DOI: **10.1016/j.jcat.2013.07.013**.

52 B. Zhang, L. Wang, Y. Zhang, Y. Ding and Y. Bi, Ultrathin FeOOH nanolayers with abundant oxygen vacancies on $BiVO_4$ photoanodes for efficient water oxidation, *Angew Chem. Int. Ed. Engl.*, 2018, **57**, 2248–2252, DOI: **10.1002/anie.201712499**.

53 S. Xie, H. Dai, J. Deng, Y. Liu, H. Yang, Y. Jiang, W. Tan, A. Ao and G. Guo, Au/3D Co_3O_4: highly active nanocatalysts for the oxidation of carbon monoxide and toluene, *Nanoscale*, 2013, **5**, 11207–11219, DOI: **10.1016/j.jcat.2013.04.025**.

54 H. Nesbitt, D. Legrand and G. Bancroft, Interpretation of Ni2p XPS spectra of Ni conductors and Ni insulators, *Phys. Chem. Miner.*, 2000, **27**, 357–366, DOI: **10.1007/s002690050265**.

55 D. Legrand, G. Bancroft and H. Nesbitt, Surface characterization of pentlandite, $(Fe,Ni)_9S_8$, by X-ray photoelectron spectroscopy, *Int. J. Miner. Process.*, 1997, 217–228, DOI: **10.1016/S0301-7516(97)00015-X**.

56 M. Ma, R. Yang, C. He, Z. Jiang, J. Shi, R. Albilali, K. Fayaz and B. Liu, Pd-based catalysts promoted by hierarchical porous Al_2O_3 and ZnO microsphere supports/coatings for ethyl acetate highly active and stable destruction, *J. Hazard. Mater.*, 2021, **401**, 123281, DOI: **10.1016/j.jhazmat.2020.123281**.

57 M. Zhang, X. Tan, T. Zhang, Z. Han and H. Jiang, The deactivation of a ZnO doped ZrO_2-SiO_2 catalyst in the conversion of ethanol/acetaldehyde to 1,3-butadiene, *RSC Adv.*, 2018, **8**, 34069–34077, DOI: **10.1039/C8RA06757K**.

58 J. Li, Z. Xu, T. Wang, X. Xie, D. Li, J. Wang, H. Huang and Z. Ao, A versatile route to fabricate Metal/UiO-66 (Metal = Pt, Pd, Ru) with high activity and stability for the catalytic oxidation of various volatile organic compounds, *Chem. Eng. J.*, 2022, **448**, 136900, DOI: **10.1016/j.cej.2022.136900**.

59 E. Groppo, J. Estephane, C. Lamberti, G. Spoto and A. Zecchina, Ethylene, propylene and ethylene oxide in situ polymerization on the $Cr(II)/SiO_2$ system: A temperature-

and pressure-dependent investigation, *Catal. Today*, 2007, **126**, 228–234, DOI: **10.1016/j.cattod.2007.01.052**.

60 X. Ding, H. Liu, J. Chen, M. Wen, G. Li, T. An and H. Zhao, In situ growth of well-aligned Ni-MOF nanosheets on nickel foam for enhanced photocatalytic degradation of typical volatile organic compounds, *Nanoscale*, 2020, **12**, 9462–9470, DOI: **10.1039/D0NR01027H**.

61 O. Mowla, E. Kennedy and M. Stockenhuber, In-situ FTIR study on the mechanism of both steps of zeolite-catalysed hydroesterification reaction in the context of biodiesel manufacturing, *Fuel*, 2018, **232**, 12–26, DOI: **10.1016/j.fuel.2018.05.096**.

62 P. Zhao, Y. Wang, Y. Jia and Y. Sheng, Theoretical investigation on the gas phase decomposition of ethyl acetate by Ni^{+}, *Struct. Chem.*, 2018, **29**, 1449–1456, DOI: **10.1007/s11224-018-1125-1**.